DOI: 10.1002/((please add manuscript number))

Article type: Communication

Anatomy of Ag/hafnia based selectors with 10^{10} nonlinearity

Rivu Midya, Zhongrui Wang, Jiaming Zhang, Sergey E. Savel'ev, Can Li, Mingyi Rao, Moon Hyung Jang, Saumil Joshi, Hao Jiang, Peng Lin, Kate Norris, Ning Ge, Qing Wu, Mark Barnell, Zhiyong Li, Huolin L. Xin, R. Stanley Williams, Qiangfei Xia*, and J. Joshua Yang**

R. Midya and Z. Wang contributed equally to this work.

R. Midya, Dr. Z. Wang, C. Li, M. Rao, Dr. M. H. Jang, Dr. S. Joshi, H. Jiang, P. Lin, Prof. Q. Xia, Prof. J. J. Yang
Department of Electrical and Computer Engineering, University of Massachusetts, Amherst, MA 01003, USA
E-mail: zhongruiwang@umass.edu; qxia@ecs.umass.edu; jjyang@umass.edu;
Dr. J. Zhang, Dr. K. Norris, Dr. N. Ge, Dr. Z. Li, Dr. R. S. Williams
Hewlett Packard Labs, Palo Alto, California 94304, USA
Prof. S. E. Savel'ev
Department of Physics, Loughborough University, Loughborough LE11 3TU, UK
Dr. Q. Wu, Dr. M. Barnell
Air Force Research Lab, Information Directorate, Rome, New York 13441, USA
Dr. H. L. Xin
Center for Functional Nanomaterials, Brookhaven National Laboratory, Upton, New York 11973, USA

Keywords: memory, memristor, selector, neuromorphic computing, nonlinearity

Abstract

Sneak path current is a significant remaining obstacle to the utilization of large crossbar arrays for non-volatile memories and other applications of memristors. A two-terminal selector device with an extremely large current-voltage nonlinearity and low leakage current could solve this problem. We present here a Ag/oxide-based threshold switching (TS) device with attractive features such as high current-voltage nonlinearity (~10^{10}), steep turn-on slope (less than 1 mV/dec), low OFF-

state leakage current (~10^{-14} A), fast turn ON/OFF speeds (<75/250 ns), and good endurance (>10^8 cycles). The feasibility of using this selector with a typical memristor has been demonstrated by physically integrating them into a multilayered 1S1R cell. Structural analysis of the nanoscale crosspoint device suggests that elongation of a Ag nanoparticle under voltage bias followed by spontaneous reformation of a more spherical shape after power off is responsible for the observed threshold switching of the device. Such mechanism has been quantitatively verified by the Ag nanoparticle dynamics simulation based on thermal diffusion assisted by bipolar electrode effect and interfacial energy minimization.

Introduction

Memristors are promising candidates for both neuromorphic computing and next generation non-volatile memory applications[1-7] because of their scalability[3, 8], 3D stacking potential[9-11], and a close resemblance to the operating characteristics of synapses[1, 4, 7, 12, 13]. These applications typically require a large crossbar array of memristors, in which sneak path currents from neighboring cells during a write or read of a target cell can severely impede the proper operation of the array. Numerous access devices coupled with a memristor at each crosspoint of the array have been introduced to tackle this critical issue[14-16]. Among those devices, a two-terminal thin-film-based selector may address the issue without compromising the scalability and 3D stacking capability of the memristor. A low OFF-current and a high selectivity of the selector are crucial to enable large crossbar arrays.

Examples of conventional two-terminal thin-film based selectors include Schottky diodes[17], tunneling junctions[18, 19], ovonic threshold switches (OTS)[20-23] and metal-insulator transitions (MIT)[24-28]. Kim et al. has demonstrated 32×32 crossbar array composed of a stacked Schottky diode and a unipolar memristor.[17] We also have recently demonstrated a highly repeatable

selector based on a crested tunnel barrier with essentially unlimited endurance,[19] but the 10^5 nonlinearity obtained in these tunneling selectors may still not be sufficient for applications where ultra-large arrays are needed. Other selectors, such as mixed-ionic-electronic conduction (MIEC)[29-31] and FAST[29, 30] have been reported with attractive performance but undisclosed materials. The concept of using engineered materials by doping fast diffusive species into dielectrics has recently been introduced[32] and demonstrated with improved nonlinearity and transition slope[33-37]. However, high operating current (e.g. >100 μA) and fast OFF-switching speed (e.g. < 500 ns) of this type of selectors have not yet been unambiguously demonstrated. Moreover, the operation mechanism, especially the RESET process in which devices relax back from their ON state to the OFF state under zero voltage bias, remains unclear. Although hypotheses based on Rayleigh instability, electronic tunneling, and opposing chemical/mechanical force has been proposed for Ag and Cu based systems in an attempt to explain the underlying RESET transition, a detailed experimental study of the microstructure and composition of the conducting channel responsible for the volatile switching is still lacking.[33, 38, 39]

We report here a new symmetric bidirectional threshold switching selector device with features including high selectivity of 10^{10}, steep turn on slope of <1 mV/dec, high endurance beyond 10^8 cycles and fast ON/OFF switch speed within 75/250 ns. The selector has been experimentally stacked on top of a Pd/Ta_2O_5/TaO_x/Pd memristor to form an integrated 1S1R cell. Microscopic analysis of a nanoscale device reveals discontinuous Ag nanostructures in a device after switching along with noticeable structural deformation and nanocrystalline *m*-HfO_2. A numerical switching model based on the thermal diffusion aided with bipolar electrode effects and Gibbs-Thomson effect or minimization of interfacial energy has been developed to quantitatively interpret the

observed switching difference between asymmetric Pd/HfO_x/Ag and symmetric Pd/Ag/HfO_x/Ag/Pd threshold devices.

Results and Discussion

Two types of Metal-Insulator-Metal (MIM) structures, asymmetric Pd/HfO_x/Ag and symmetric Pd/Ag/HfO_x/Ag/Pd cross-point stacks, were prepared as schematically illustrated in **Figure 1(a)** for both. (See Experimental Section). The as-prepared Pd/HfO_x/Ag MIM junctions were in their high resistance state (HRS) or OFF-state. The OFF resistance of the as-prepared device was about 10^{13} ohms at 0.1 V. The device needed to be electroformed at 1.8 V and a 1 µA compliance current to become operational. The current of the device increased abruptly, but then returned to the HRS while sweeping the voltage back to zero. In the next positive sweep after electroforming process, the device switched ON at a much lower voltage (0.4 V). Figure 1(b) presents 100 consecutive cycles of such TS behavior. The device was able to conduct a surprisingly high current of 1 mA while still retaining volatile behavior. The HRS notch around 0.06V in Figure 1(b) corresponds to a negative current that can be attributed to the nano-battery effect[40]. By setting the read voltage (V_{read}) to 0.2 V and the half-read voltage ($V_{read}/2$) to 0.1 V, the 100 switching cycles in Figure 1 (b) yield a selectivity of ~10^{10} in terms of the median currents at the two voltages and a maximum selectivity of 6×10^{11}, which is the highest reported in any type of selector so far[29, 30]. The turn-ON slope was <1 mV/decade, which is also the sharpest reported so far[34]. Symmetrical bi-directional volatile switching was observed in a structurally symmetric Pd/Ag/HfO_x/Ag/Pd stack, as shown in Figure 1(c) where devices show no noticeable deterioration after 100 cycles. Both devices feature a low OFF current of 10^{-14} A (at 0.1 V), which is also the lowest reported so far.[33] A device-to-device variation on the same wafer was tested on ten devices. (See Supplementary Information Figure S1(a)) All devices have shown repeatable threshold switching with mean

threshold voltages spanning from -0.5V to -0.3V and 0.4V to 0.7V, for negative and positive polarities respectively. (Extracted from quasi-DC sweeps, see Supplementary Information Figure S1(b-c))

The fastest switching observed in these devices exhibited a transition from high resistance state (HRS) to a low resistance state (LRS) within 75 ns when a 2 V pulse was applied, which is comparable to that of a typical memristor,[10] and relaxation back to the HRS within 250 ns after the bias was removed, as indicated by **Figure 2(a)**. Note that the turn-ON time could be shorter than 75 ns with a pulse of a higher magnitude, given that the turn-ON time is inversely proportional to the exponential of the amplitude of the driving voltage pulse as reported for CBRAM[41]. The device exhibited an endurance over a hundred million cycles. Figure 2(b) shows the endurance testing result that was acquired using 10 μs/4V programming pulses and 75 μs/0.1V read pulses, with a 25 μs wait time in between each write and read event (see the inset of Figure 2(b)). The delay time follows a distribution at a given voltage and hence an elongated pulse was employed for the endurance test to minimize the unsuccessful switching events. (See Supplementary Information Figure S2(a)). In addition, relaxation time typically maintains a linear relationship with the pulse width. (See Supplementary Information Figure S2(b)). The threshold switching at an elevated temperature displays an increased OFF state current due to thermal facilitated transport.[30, 42, 43] (See Supplementary Figure S3(a-b)) The relaxation time (or equivalently the retention time) of the Pd/Ag/HfO_x/Ag/Pd selectors follows a typical exponential relationship with the reciprocal temperature (See Supplementary Figure S3(c)), yielding a fitted Ag hopping barrier of 0.21 eV, which is close to that in a Ag doped silicon oxynitride.[44]

We fabricated a vertically integrated cell consisting of a Pd/Ag/HfO_x/Ag/Pd threshold switch on top of a Pd/Ta_2O_5/TaO_x/Pd memristor with a Pd layer as a shared middle electrode (ME), as shown

in a scanning electron micrograph for a top view and a transmission electron micrograph for a focused ion beam cut cross-section (**Figure 3(a)**). The dedicated middle electrode allowed us to access the characteristics of the selector, the memristor and the 1S1R cell, separately. Electrical DC voltage sweeps had been applied to the individual Pd/Ag/HfO_x/Ag/Pd threshold selector, as shown in Figure 3(b). The selector showed repeatable threshold switching with both biasing polarities. Repeatable bipolar memristive switching of the individual Pd/Ta_2O_5/TaO_x/Pd memristor is illustrated in Figure 3(c). Figure 3(d) shows the DC voltage sweep response of the integrated 1S1R. The Pd/Ag/HfO_x/Ag/Pd threshold switch acted as a select device in this case, with the capability of greatly suppressing sneak current in large arrays. With increasing voltage, the selector first turned on at ~0.5 V followed by the SET transition of the Pd/Ta_2O_5/TaO_x/Pd memristor at ~1.2 V. The subsequent reading sweep with the same single sweep (purple curve) verified the LRS of the memristor. During the negative voltage sweep, the threshold selector turned on at ~-0.4 V followed by a gradual RESET transition of the Pd/Ta_2O_5/TaO_x/Pd memristor in the interval from ~-0.8V to ~-1.4V. (See the blue curve) The following reading sweep (magenta curve) again verified the HRS of the memristor. Similar electrical performances had also been demonstrated on wire-joined 1S1R system consisting of discrete Pd/Ag/HfO_x/Ag/Pd threshold selector and the same kind of Pd/Ta_2O_5/TaO_x/Pd memristors. (See Supplementary Information Figure S4) It should also be noted that the threshold voltage to turn on a Pd/Ag/HfO_x/Ag/Pd threshold switch with a given voltage pulse is a function of the pulse width. The shorter the pulse width used, the larger the switching voltage needed. (See for example, Figure 2) Thus, the threshold voltages for the selectors using fast pulses are higher than those above values obtained from the quasi-DC switching sweeps.

To unravel the underlying mechanism of the volatile switching, nanoscale crosspoint junctions with an electrode width of 100 nm were fabricated for high resolution transmission electron microscopy (HRTEM) analysis (see **Figure 4(a)**). The TEM sample was prepared to cover the entire nanodevice to minimize the possibility of missing important features responsible for the switching behavior. The nanoscale Pd/Ag/HfO_x/Ag/Pd crosspoint device demonstrated similar threshold switching characteristics to the microdevices prepared by photolithography, and withstand an ON-state current of 100 µA (see Supplementary Information Figure S5). In order to observe the evolution of the microstructures, Figure 4(c) and (d) show two cross-sections of nanoscale junctions of an as-deposited device and an electrically operated device that exhibited repeated volatile switching as shown in Figure 4(b). The metal/dielectric interface in the operated device was rougher than that of the as-deposited device, a possible result of grain growth in the electrodes induced by Joule heating.[45] In addition, the Energy Dispersive Spectroscopy (EDS) elemental map revealed that Ag layers at both the top and bottom electrodes in the operated device (Figure 4(d)) were less continuous, compared to the Ag layers in Figure 4(c) of the as-deposited device, which is likely caused by Ag migration into both the dielectric and electrode layers during electrical cycling[46]. As highlighted by the two white arrows, the Ag profile of the EDS maps in the operated device revealed two detectable Ag protrusions with a cone-like shape, one residing in the top electrode pointing downwards while the other standing on the bottom electrode pointing upwards. Being a poor Ag ion conductor and unable to dissolve Ag chemically, HfO_x makes Ag^+ easy to be chemically reduced within the dielectrics due to low ion mobility and low redox reaction rate, yielding the observed cone shaped Ag filament which grows from the Ag source rather than having Ag deposition on the opposite anode.[47, 48] However, neither of the protrusions completely bridged the dielectric between the top and bottom electrodes, which is different from the behavior

typically observed in CBRAM[46, 48, 49]. The incomplete bridging was further verified by EDS line scans of the Ag peak along the white dashed lines shown in Figure 4(e), which also showed a clear narrowing of the dielectric layer thickness. This agrees with the experimental observation that those devices relax back to the HRS after the switching voltage is removed. In addition, the nanocrystalline monoclinic phase of HfO_2 was observed adjacent to the broken bridge (see Figure 4(f)), a common aftereffect of Joule heating during the operation of the device[50].

In the light of the observed microstructure of the volatile switch, we developed a switching model based on both the Gibbs-Thomson effect, interfacial energy minimization[40, 51-54] and migration of Ag nanoclusters due to both thermal driven diffusion and bipolar electrode effects[47, 49], to quantitatively interpret the observed threshold switching in both asymmetric Pd/HfO_x/Ag and symmetric Pd/Ag/HfO_x/Ag/Pd threshold selectors.[44] This model links electrical, nano-mechanical and heat degrees of freedom. **Figure 5(a)** shows the simulated unipolar threshold switching of a Pd/HfO_x/Ag device, which replicates the IV characteristics observed in the original Figure 1(b). The pristine device has a vertical Ag atom distribution illustrated by Figure 5(b1) where Ag is confined within the electrode. With a positive voltage applied, there are one or more regions in the cell where current flows preferentially. A localized area is heated due to the flow of the current, and this thermal channel provides a region for a preferential diffusion of Ag away from a clump towards the opposite electrode via a diffusion process aided by the bipolar electrode effect. This will decrease the resistance and enable more current to flow till reach the compliance conductance and the Ag atoms form a connected filament bridging both electrodes as shown in Figure 5(b2). Lowering of the applied voltage will cause spontaneous recovery of the conductance back toward zero (See Figure 5(b3)) because nanoscale Ag filament connecting two electrodes bears a large chemical potential (or large interfacial energy) due to the Gibbs-Thomson effect and

such high potential is unstable and will be released upon the ceasing of the electrical power. (See Supplementary Information Figure S6) In addition, the dissolution of the filament may also be influenced by the observed Nernst potential, diffusion potential, together with Gibbs-Thomson effect, which constitute the nano-battery effect.[40, 53] (See Supplementary Information Figure S7) This threshold switching process of Pd/HfO_x/Ag selector is schematically illustrated by Figure 5(e) as well. However, with a reversed biasing polarity, the Ag would not fill the gap due to the dominant bipolar electrode effect over thermal driven diffusion, as shown by the Figure 5(b4-b6). This differs from a symmetric Pd/Ag/HfO_x/Ag/Pd threshold selector which exhibits nonpolar switching as depicted by Figure 5(c) (similar to Figure 1(c)). With positive voltage applied on the top electrode of the Pd/Ag/HfO_x/Ag/Pd selector, the Ag from the top electrode will migrate to the gap region to form the conductive filament. (See Figure 5(d1-d3)) Unlike the unipolar Pd/HfO_x/Ag threshold selector, applying and then removing a negative biasing voltage will first drive Ag from the bottom electrode to the gap region and then back, (See Figure 5(d4-d6)) which is responsible for the observed threshold switching with negative biasing. This threshold switching process in a Pd/Ag/HfO_x/Ag/Pd selector is schematically summarized in Figure 5(e). It is worthy to note that where the Ag cluster finally resides depends on the mobility of Ag atoms in the host matrix, the thinness of the dielectric layer and the ambient temperature. In case of a relatively low mobility, thick dielectric layer and fast temperature decay, the Ag atoms may only be able to migrate to local energy-minimal positions within the dielectric layer rather than a global energy minimization configuration of the system. This results in spherical clusters of Ag atom distributed within the dielectric layer, as observed in both the Au/SiO_xN_y:Ag/Au and Ag/HfO_x/Ag lateral volatile switches (See Supplementary Information Figure S8 and S9). However, if the mobility is

sufficiently high, the dielectric layer is thin and the temperature decays slowly, Ag atoms may be able to diffuse to the electrodes and form protrusions on the surfaces of the electrodes.

Conclusion

We have shown exceptional selection characteristics in Ag based oxide TS devices. Steep slope of <1mV/decade, high selectivity of 10^{10}, high current level of mA and fast ON/OFF of less than 75/250 ns were achieved simultaneously in a device by spontaneously rupture of Ag conduction filament(s) upon voltage removal facilitated by Gibbs-Thomson effect or minimization of the interfacial energy as both revealed by the microscopic structural analysis and Ag nanoparticle dynamics simulation. The integration feasibility of such selector with a memristor has been demonstrated by fabricating 1S1R integrated devices, which could benefit numerous applications with large crossbar arrays, including non-volatile memory and neuromorphic computing.

Experimental Section

HfO_x threshold selector fabrication: Both types of Metal-Insulator-Metal (MIM) structures were prepared on a p-type (100) Si wafer with 100 nm thermal oxide. The Pd/HfO_x/Ag crosspoint stack with a 5×5 μm^2 junction consists of 20 nm thick evaporated Pd(Ag) bottom(top) electrodes patterned by photolithography. The 5 nm thick HfO_x dielectric was deposited by atomic layer deposition (ALD) at 150°C using water and tetrakis(dimethylamino)hafnium as precursors. The symmetric Pd/Ag/HfO_x/Ag/Pd junction was deposited using the same techniques with 3.2 nm Ag and 20 nm Pd layers. A nanoscale crosspoint version of the Pd/Ag/HfO_x/Ag/Pd junction was fabricated by using e-beam lithography with all other procedures unaltered from those of the microdevice fabrication.

Integrated 1S1R cell fabrication: For the integrated device, Pd bottom electrodes of 30 nm thickness (BE) were evaporated onto the SiO_2 substrate with a 2 nm thick Ta adhesion layer. A 10 nm thick blanket Ta_2O_5 switching layer of the memristor was then deposited by sputtering a Ta_2O_5 target in Ar plasma. Middle electrodes consisting of 10 nm reduced TaO_x followed by 40 nm Pd, were evaporated afterwards. A 10 nm SiO_2 buffer layer is grown by sputtering a SiO_2 target in Ar plasma and then subjected to reactive ion etching (mixed CHF_3 and O_2 gas plasma) to open via contacts to the middle electrodes. A 3.2 nm Ag layer was evaporated followed by the lift off of the photoresist of the contact via hole. A 5 nm thick HfO_x blanket switching layer of the threshold selector was deposited by atomic layer deposition at 200 °C. Top electrodes (TE) of 3.2 nm Ag and 40 nm thick Pd were evaporated.

Nano-gap Au/SiO_xN_y:Ag/Au junction fabrication: For the nano-gap planar Au/SiO_xN_y:Ag/Au device, the 15 nm SiO_xN_y:Ag layer was sputter-deposited at room temperature using a Si target in an ambience of mixed Ar, O_2, and N_2. Au electrodes were patterned by electron beam lithography, followed by evaporation of a 20 nm thick Au layer on top of 2 nm Ti adhesion layer. A second layer of dielectrics was then deposited in the same manner as the foundation layer but with an increased thickness of 20 nm.

Nano-gap Ag/HfO_x/Ag junction fabrication: For the nano-gap planar Ag/HfO_x/Ag device, the bottom 10 nm HfO_x layer was grown by ALD at 200 °C. Ag was evaporated onto the HfO_x layer with a 2 nm Ge seed layer patterned by electron beam lithography. The top 10 nm HfO_x layer was deposited in the same manner with that of the bottom HfO_x layer.

Electrical measurements: DC voltage sweeps were performed using a Keysight B1500A semiconductor device analyser equipped with High Resolution Source and Measurement Units to sense the current with an integration time of 16 power line cycles with a specified resolution of 1 fA. Time domain voltage pulse operation and fast current sense is carried by a Keysight B1530A Waveform Generator/Fast Measurement Unit with a maximum noise (effective resolution) 0.2% of the selected current measurement range. For the device delay and relaxation speed measurement, one channel of the Keysight B1530A applied voltage and the other channel acquired the current value. For the endurance measurement, a 3.9 MΩ resistor was in series with the device to limit the ON-state current.

Transmission Electron Microscopy: Aberration-corrected STEM/EELS analysis was performed with a FEI Titan transmission electron microscopy (TEM) at an accelerating voltage of 300 KV.

Ag nanoparticles dynamics simulation To simulate both symmetric and asymmetric memristors, we adopted the model which has successfully described memristors with diffusive dynamics.[44] The model links electrical, nano-mechanical and heat degrees of freedom. The diffusion of Ag nano-clusters can be described by a Langevin equation

$$\eta \frac{dx_i}{dt} = -\frac{\partial U(x_i)}{\partial x_i} + \alpha \frac{V(t)}{L} + \sqrt{2\eta k_B T}\, \xi_i, \quad (1)$$

where positions x_i describe cluster locations inside the HfO2 layer at time t, η is cluster viscosity, U is the potential energy, the term $\alpha \frac{V(t)}{L}$ describes the electrical force when the voltage $V(t)$ is applied across the memristor of size $2L$ and a charge α is induced in Ag clusters. The last term represents a random force acting on clusters with white noise ξ_i(i.e., $\langle \xi_i \rangle = 0, \langle \xi_i(0)\xi_i(t) \rangle = \delta(t)$)

fluctuations, while the noise amplitude is controlled by the cluster temperature T (here k_B is the Boltzmann constant). Here we focus on influence of asymmetry on the conductance-voltage loops, and thus, we consider contribution of the interfacial energy to the potential $U_I = -w_I \exp\left(-\frac{(x_i-x_0)^2}{R_I^2}\right)$ near Ag bulk side of the device and a weak repulsive potential $U_{Pd} = w_{Pd}\exp\left(-\frac{L-x}{R_{Pd}}\right)$ from the Pd bulk side. Therefore, $U = U_I(x_0 = -0.85L) + U_{Pd}$ for asymmetric device (Ag/HfO2/Pd) and $U = U_I(x_0 = -0.85L) + U_I(x_0 = 0.85L)$ for symmetric one (Ag/HfO2/Ag) with ratio $w_I/w_{Pd} = 0.9$, $\frac{R_{Pd}}{R_I} = 3$. To avoid unnecessary delay in simulations we here ignore pinning potential responsible for relaxation of the diffusive memristor.[44]

The temperature relaxation is described by the Newton's cooling law:

$$\frac{dT}{dt} = C_T Q - \kappa(T - T_0), \quad (2)$$

with the Joule heating power $Q = V^2/R_M$, heat capacitance C_T, the heat transfer coefficient κ and the background cluster temperature T_0 chosen to be 0.063 w_I/k_B to avoid spontaneous excitation of the memristor to its low resistance state at zero applied voltage. On the other hand, the induced charged was chosen such that it reduces the activation barrier to its low resistance state by factor 2 and the heat capacitance was chosen such that the effective cluster temperature is of the order of the potential wells in the memristor low resistive state (note that the actual system temperature and the macroscopic-cluster temperature can be significantly different). All times in simulations were measured in temperature relaxation time $1/\kappa$ and sweep time was chosen $1000/\kappa$ to ensure that sweeping is slower than all relaxation processes.

Supporting Information

Supporting Information is available from the Wiley Online Library or from the author.

Acknowledgements

R. M. and Z. W. contributed equally to this work. This work was supported in part by the U.S. Air Force Research Laboratory (AFRL) (Grant No. FA8750-15-2-0044), U.S. Air Force Office for Scientific Research (AFOSR) (Grant No. FA9550-12-1-0038), and the National Science Foundation (NSF) (ECCS-1253073). Any opinions, findings and conclusions or recommendations expressed in this material are those of the authors and do not necessarily reflect the views of AFRL. Part of the device fabrication was conducted in the clean room of Center for Hierarchical Manufacturing (CHM), an NSF Nanoscale Science and Engineering Center (NSEC) located at the University of Massachusetts Amherst.

Received: ((will be filled in by the editorial staff))
Revised: ((will be filled in by the editorial staff))
Published online: ((will be filled in by the editorial staff))

References

[1] R. Waser and M. Aono, *Nat. Mater.*, **2007,** 6, 833.

[2] R. Waser, R. Dittmann, G. Staikov, and K. Szot, *Adv. Mater.*, **2009,** 21, 2632.

[3] D.-H. Kwon, K. M. Kim, J. H. Jang, J. M. Jeon, M. H. Lee, G. H. Kim, X.-S. Li, G.-S. Park, B. Lee, S. Han, M. Kim, and C. S. Hwang, *Nat. Nanotechnol.*, **2010,** 5, 148.

[4] T. Ohno, T. Hasegawa, T. Tsuruoka, K. Terabe, J. K. Gimzewski, and M. Aono, *Nat. Mater.*, **2011,** 10, 591.

[5] A. B. Chen, S. G. Kim, Y. Wang, W. S. Tung, and I. W. Chen, *Nat. Nanotechnol.*, **2011,** 6, 237.

[6] B. J. Choi, A. B. Chen, X. Yang, and I. W. Chen, *Adv. Mater.*, **2011,** 23, 3847.

[7] J. J. Yang, D. B. Strukov, and D. R. Stewart, *Nat. Nanotechnol.*, **2013,** 8, 13.

[8] K. Terabe, T. Hasegawa, T. Nakayama, and M. Aono, *Nature*, **2005,** 433, 47.

[9] D. B. Strukov and R. S. Williams, *Proc. Natl. Acad. Sci. U.S.A.*, **2009,** 106, 20155.

[10] S. Yu, H.-Y. Chen, B. Gao, J. Kang, and H. S. P. Wong, *ACS Nano*, **2013,** 7, 2320.

[11] J. Y. Seok, S. J. Song, J. H. Yoon, K. J. Yoon, T. H. Park, D. E. Kwon, H. Lim, G. H. Kim, D. S. Jeong, and C. S. Hwang, *Adv. Funct. Mater.*, **2014,** 24, 5316.

[12] H. Lim, I. Kim, J. S. Kim, C. S. Hwang, and D. S. Jeong, *Nanotechnology*, **2013,** 24, 384005.

[13] D. Mahalanabis, H. J. Barnaby, Y. Gonzalez-Velo, M. N. Kozicki, S. Vrudhula, and P. Dandamudi, *Solid·State Electron.*, **2014,** 100, 39.

[14] S. Kim, J. Zhou, and W. D. Lu, *IEEE Trans. Elect. Dev.*, **2014,** 61, 2820.

[15] J. Zhou, K. H. Kim, and W. Lu, *IEEE Trans. Elect. Dev.*, **2014,** 61, 1369.

[16] G. W. Burr, R. S. Shenoy, and H. Hwang, in *Resistive Switching*, (Eds: D. Ielmini and R. Waser: Wiley-VCH Verlag GmbH & Co. KGaA, **2016**, 623.

[17] G. H. Kim, J. H. Lee, Y. Ahn, W. Jeon, S. J. Song, J. Y. Seok, J. H. Yoon, K. J. Yoon, T. J. Park, and C. S. Hwang, *Adv. Funct. Mater.*, **2013,** 23, 1440.

[18] A. Kawahara, R. Azuma, Y. Ikeda, K. Kawai, Y. Katoh, Y. Hayakawa, K. Tsuji, S. Yoneda, A. Himeno, K. Shimakawa, T. Takagi, T. Mikawa, and K. Aono, *IEEE J. Solid-St. Circ.*, **2013,** 48, 178.

[19] B. J. Choi, J. Zhang, K. Norris, G. Gibson, K. M. Kim, W. Jackson, M. X. Zhang, Z. Li, J. J. Yang, and R. S. Williams, *Adv. Mater.*, **2016,** 28, 356.

[20] M. Anbarasu, M. Wimmer, G. Bruns, M. Salinga, and M. Wuttig, *Appl. Phys. Lett.*, **2012,** 100, 143505.

[21] M. J. Lee, D. Lee, H. Kim, H. S. Choi, J. B. Park, H. G. Kim, Y. K. Cha, U. I. Chung, I. K. Yoo, and K. Kim, in *Electron Devices Meeting (IEDM), 2012 IEEE International*, **2012**. 2.6.1.

[22] S. Kim, Y. B. Kim, K. M. Kim, S. J. Kim, S. R. Lee, M. Chang, E. Cho, M. J. Lee, D. Lee, C. J. Kim, U. I. Chung, and I. K. Yoo, in *VLSI Technology (VLSIT), 2013 Symposium on*, **2013**. T240.

[23] M. J. Lee, D. Lee, S. H. Cho, J. H. Hur, S. M. Lee, D. H. Seo, D. S. Kim, M. S. Yang, S. Lee, E. Hwang, M. R. Uddin, H. Kim, U. I. Chung, Y. Park, and I. K. Yoo, *Nat. Commun.*, **2013,** 4, 2629.

[24] M. Son, J. Lee, J. Park, J. Shin, G. Choi, S. Jung, W. Lee, S. Kim, S. Park, and H. Hwang, *IEEE Elect. Dev. Lett.*, **2011,** 32, 1579.

[25] S. Kim, X. Liu, J. Park, S. Jung, W. Lee, J. Woo, J. Shin, G. Choi, C. Cho, S. Park, D. Lee, E. j. Cha, B. H. Lee, H. D. Lee, S. G. Kim, S. Chung, and H. Hwang, in *VLSI Technology (VLSIT), 2012 Symposium on*, **2012**. 155.

[26] E. Cha, J. Woo, D. Lee, S. Lee, J. Song, Y. Koo, J. Lee, C. G. Park, M. Y. Yang, K. Kamiya, K. Shiraishi, B. Magyari-Köpe, Y. Nishi, and H. Hwang, in *Electron Devices Meeting (IEDM), 2013 IEEE International*, **2013**. 10.5.1.

[27] D. Lee, J. Park, S. Park, J. Woo, K. Moon, E. Cha, S. Lee, J. Song, Y. Koo, and H. Hwang, in *Electron Devices Meeting (IEDM), 2013 IEEE International* **2013**. 10.7.1.

[28] G. A. Gibson, S. Musunuru, J. Zhang, K. Vandenberghe, J. Lee, C.-C. Hsieh, W. Jackson, Y. Jeon, D. Henze, Z. Li, and R. Stanley Williams, *Appl. Phys. Lett.*, **2016,** 108, 023505.

[29] S. H. Jo, T. Kumar, S. Narayanan, W. D. Lu, and H. Nazarian, in *Electron Devices Meeting (IEDM), 2014 IEEE International*, **2014**. 6.7.1.

[30] S. H. Jo, T. Kumar, S. Narayanan, and H. Nazarian, *IEEE Trans. Electron Dev.*, **2015,** 62, 3477.

[31] P. Narayanan, G. W. Burr, R. S. Shenoy, S. Stephens, K. Virwani, A. Padilla, B. N. Kurdi, and K. Gopalakrishnan, *IEEE J. Electron Devices Soc.*, **2015,** 3, 423.

[32] J. Yang, W. Wu, and Q. Xia, United States Patent 8,879,300, **2014**.

[33] Q. Luo, X. Xu, H. Liu, H. Lv, N. Lu, T. Gong, S. Long, Q. Liu, H. Sun, W. Banerjee, and M. Liu, in *Electron Devices Meeting (IEDM), 2015 IEEE International*, **2015**. 10.4.1.

[34] J. Song, J. Woo, A. Prakash, D. Lee, and H. Hwang, *IEEE Elect. Dev. Lett.*, **2015,** 36, 681.

[35] J. Song, A. Prakash, D. Lee, J. Woo, E. Cha, S. Lee, and H. Hwang, *Appl. Phys. Lett.*, **2015,** 107, 113504.

[36] W. Chen, H. J. Barnaby, and M. N. Kozicki, *IEEE Elect. Dev. Lett.*, **2016,** 37, 580.

[37] J. Song, J. Woo, S. Lee, A. Prakash, J. Yoo, K. Moon, and H. Hwang, *IEEE Elect. Dev. Lett.*, **2016,** PP, 1.

[38] C.-P. Hsiung, H.-W. Liao, J.-Y. Gan, T.-B. Wu, J.-C. Hwang, F. Chen, and M.-J. Tsai, *ACS Nano*, **2010,** 4, 5414.

[39] H. Sun, Q. Liu, C. Li, S. Long, H. Lv, C. Bi, Z. Huo, L. Li, and M. Liu, *Adv. Funct. Mater.*, **2014,** 24, 5679.

[40] I. Valov, E. Linn, S. Tappertzhofen, S. Schmelzer, J. van den Hurk, F. Lentz, and R. Waser, *Nat. Commun.*, **2013,** 4, 1771.

[41] S. Yu and H. S. P. Wong, *IEEE Trans. Elect. Dev.*, **2011,** 58, 1352.

[42] Z. Wang, H. Yu, X. A. Tran, Z. Fang, J. Wang, and H. Su, *Phys. Rev. B*, **2012,** 85.

[43] Z. Wang, H. Yu, and H. Su, *Sci. Rep.*, **2013,** 3, 3246.

[44] Z. Wang, S. Joshi, S. E. Saveliev, H. Jiang, R. Midya, P. Lin, M. Hu, N. Ge, J. P. Strachan, Z. Li, Q. Wu, M. Barnell, G.-L. Li, H. L. Xin, R. S. Williams, Q. Xia, and J. J. Yang, *Nat. Mater.*, **2016,** DOI:10.1038/nmat4756.

[45] B. Günther, A. Kumpmann, and H. D. Kunze, *Scr. Metall. Mater.*, **1992,** 27, 833.

[46] Y. C. Yang, F. Pan, Q. Liu, M. Liu, and F. Zeng, *Nano Lett.*, **2009,** 9, 1636.

[47] Y. Yang, P. Gao, L. Li, X. Pan, S. Tappertzhofen, S. Choi, R. Waser, I. Valov, and W. D. Lu, *Nat. Commun.*, **2014,** 5, 4232.

[48] Y. Yang, P. Gao, S. Gaba, T. Chang, X. Pan, and W. Lu, *Nat. Commun.*, **2012,** 3, 732.

[49] X. Tian, S. Yang, M. Zeng, L. Wang, J. Wei, Z. Xu, W. Wang, and X. Bai, *Adv. Mater.*, **2014,** 26, 3649.

[50] F. Miao, J. P. Strachan, J. J. Yang, M. X. Zhang, I. Goldfarb, A. C. Torrezan, P. Eschbach, R. D. Kelley, G. Medeiros-Ribeiro, and R. S. Williams, *Adv. Mater.*, **2011,** 23, 5633.

[51] I. Valov and G. Staikov, *J. Solid State Electrochem.*, **2012,** 17, 365.

[52] J. van den Hurk, E. Linn, H. Zhang, R. Waser, and I. Valov, *Nanotechnology*, **2014,** 25, 425202.

[53] S. Tappertzhofen, E. Linn, U. Böttger, R. Waser, and I. Valov, *IEEE Elect. Dev. Lett.*, **2014,** 35, 208.

[54] D. M. Guzman, N. Onofrio, and A. Strachan, *J. Appl. Phys.*, **2015,** 117, 195702.

Figure Captions

Figure 1 HfO_x based TS devices showing threshold switching with a large ON/OFF ratio and a steep slope. (a) Schematics of the asymmetric and symmetric device structures. The inset shows an SEM image of the crosspoint device. (b) The DC I-V characteristic of the Pd/HfO_x/Ag selector yields a selectivity of 10^{10}. (c) Consecutive 50 cycles of DC voltage sweep with positive biasing followed by 50 cycles of DC sweep with negative biasing on Pd/Ag/HfO_x/Ag/Pd showing bipolar threshold switching behavior with an ON/OFF ratio of 10^8 (d) Device shows an ON switching slope of ~1mV/decade.

Figure 2 switching speed and endurance performance of the bipolar Pd/Ag/HfO_x/Ag/Pd selectors. (a) The device is turned on within 75 ns and relaxes back to HRS within 250 ns. (b) Endurance of the selector with over 10^8 cycles. The inset shows the waveform employed in endurance measurement which consists of a 10 µs pulse with an amplitude of 4 V for ON switching followed by a 0.1 V read pulse. The time interval between switching pulses is 100 µs (25 µs waiting time plus 75 µs read time). A series resistor of 3.9 MΩ was used to limit the ON-state current.

Figure 3 Electrical performance of an integrated 1S-1R device consisting of a Pd/Ta_2O_5/TaO_x/Pd memristor and a Pd/Ag/HfO_x/Ag/Pd selector. (a) Scanning electron micrograph top view of the vertically integrated selector and memristor (left) and transmission electron micrograph of the cross-section prepared by focused ion beam cutting. (b) Repeatable bipolar threshold switching of the individual Pd/Ag/HfOx/Ag/Pd selector. (c) Repeatable bipolar memristive switching of the individual Pd/Ta_2O_5/TaO_x/Pd memristor. (d) DC I-V characteristics of the vertically integrated selector and memristor. The selector turned on at ~0.5V (blue curve), followed by the SET of the memristor at ~1.2V. The LRS of memristor was verified by the subsequent sweep (purple curve). On the negative voltage, the selector turned on at ~-0.4V (red curve) before the memristor RESET

in the interval from ~-0.8V to ~-1.2V. The followed sweep verified the HRS of the memristor (magenta curve).

Figure 4 Anatomy of nanodevices revealing morphology, composition and structural information around filament remains. (a) SEM micrograph of 100 nm crosspoint junctions of Pd/Ag/HfO_x/Ag/Pd selectors. (b) DC I-V characteristics of the junction on the right side of (a) showing repeatable threshold switching. (c) TEM cross-sectional image of a pristine device. The inset shows an EDS map of Ag element of the solid white box region. (d) TEM cross-sectional image of the measured device with IV shown in (b). The inset shows an EDS map of Ag element of the solid white box region. Two Ag protrusions are highlighted by the white arrows which are likely the remains of filaments. (e) EDS line profile of Ag along the dashed white lines in (c) and (d). The measured device features a narrow Ag gap as a result of the occurrence of Ag protrusion. (f) HRTEM of the dashed white box region in (d) which shows a narrowed Ag gap. The FFT (Fast Fourier Transfer) corresponding to the left white box shows the presence of nanocrystalline Ag while that of the right box shows the existence of crystalline HfO_2 [011] facets.

Figure 5 Simulated operation of both asymmetric Pd/HfO_x/Ag unipolar threshold selector and symmetric Pd/Ag/HfO_x/Ag/Pd selector devices. (a) Simulated unipolar threshold switching of an asymmetric Ag/HfO_x/Pt threshold switch upon both positive and negative DC voltage sweeps. The sweep sequence is indicated by the blue arrows (b) Evolution of Ag atom density along the vertical direction of device. Each distribution was averaged over time $0.2/\kappa$ and instantaneous particle snapshots (dots) at time moments indicated by orange dots in (a). (c) Simulated nonpolar threshold switching of a symmetric Pd/Ag/HfO_x/Ag/Pd selector upon both positive and negative DC voltage sweeps. The sweep sequence is indicated by the blue arrows (d) Evolution of Ag atom density along the vertical direction of device. Each distribution was averaged over time $0.2/\kappa$ and instantaneous particle snapshots (dots) at time moments indicated by orange dots in (c). (e) Schematic illustration of the volatile switching

process in both asymmetric Ag/HfO_x/Pt unipolar threshold selector device and symmetric Pd/Ag/HfO_x/Ag/Pd selector device.

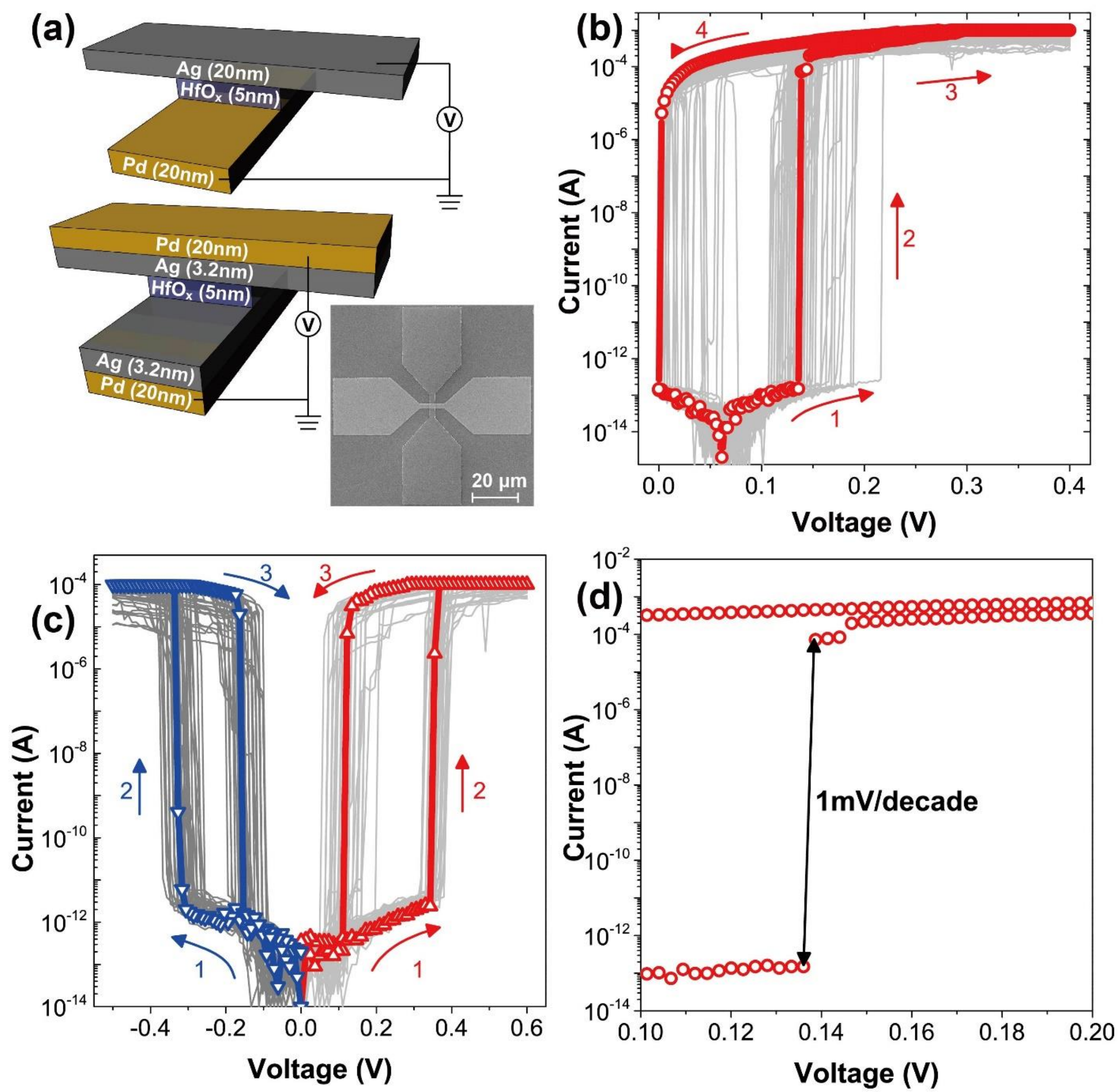

Figure 1

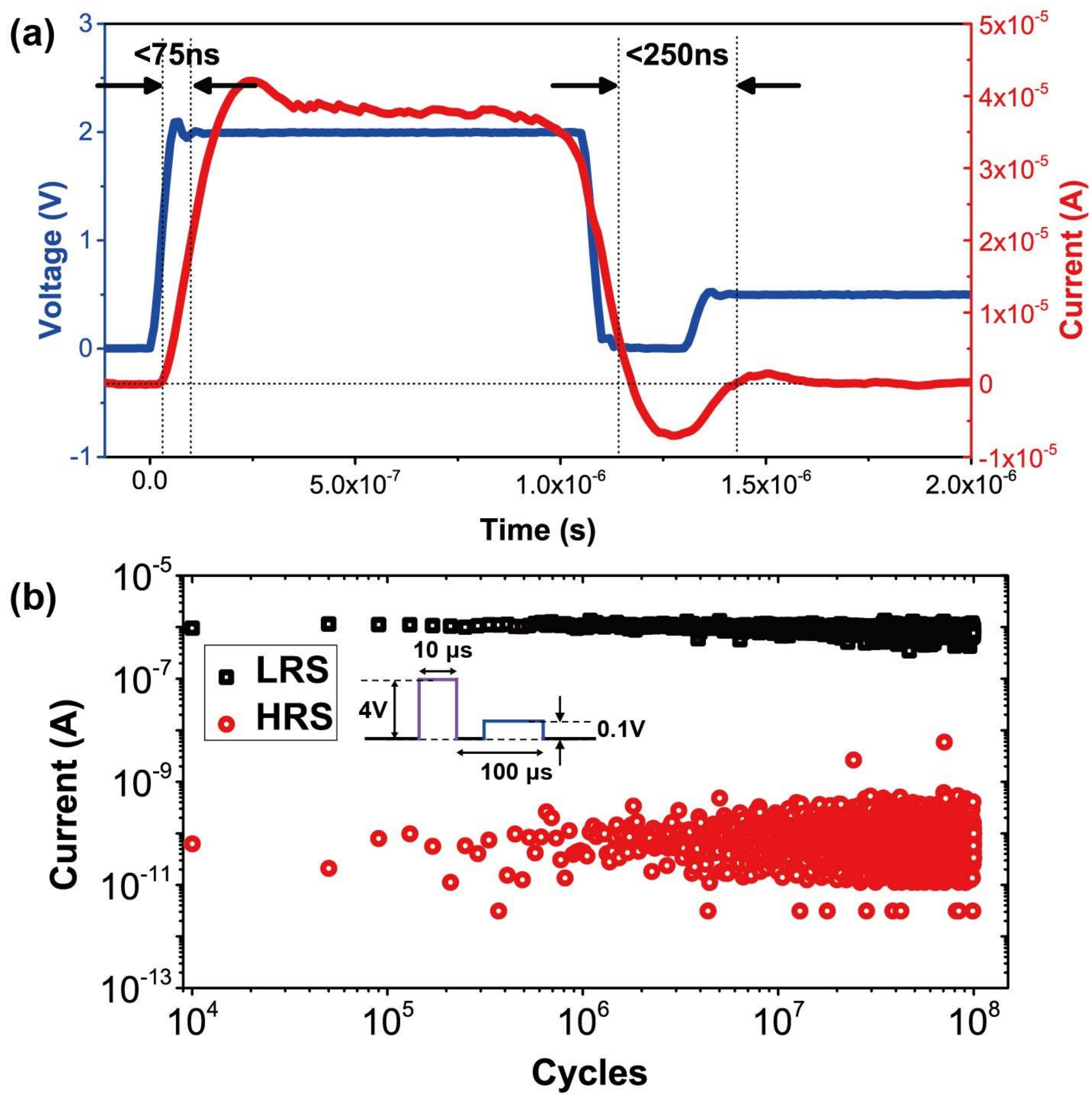

Figure 2

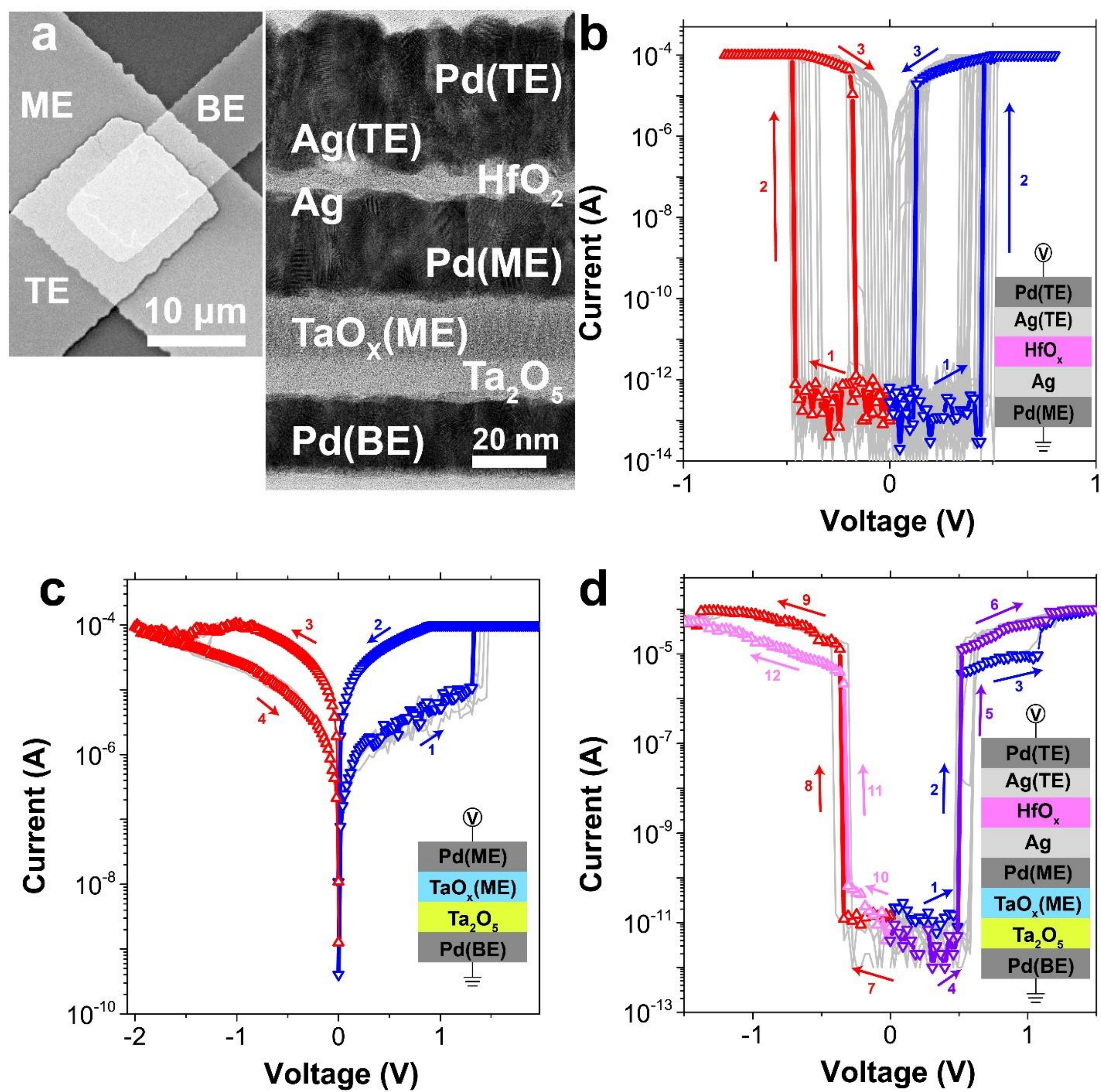

Figure 3

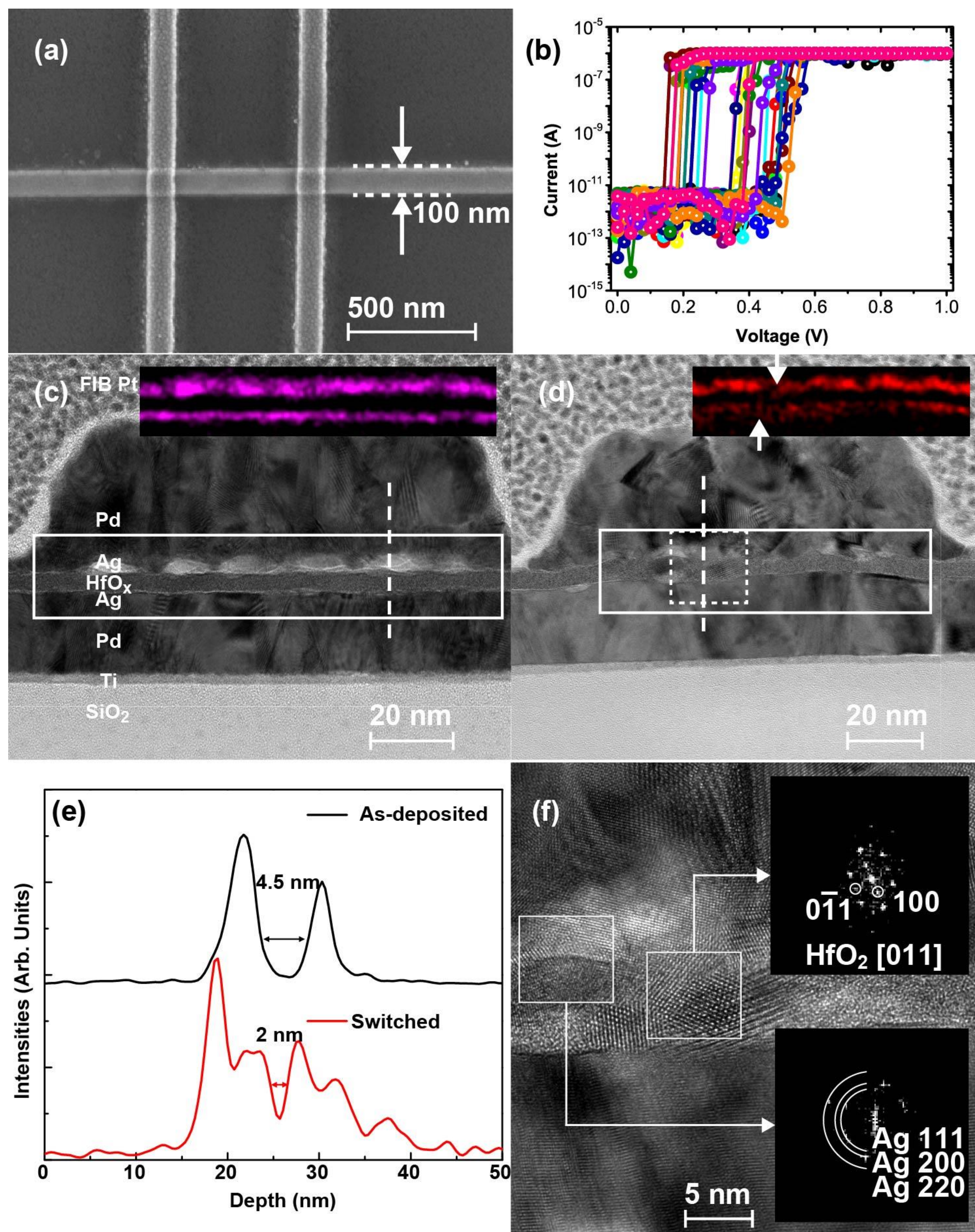

Figure 4

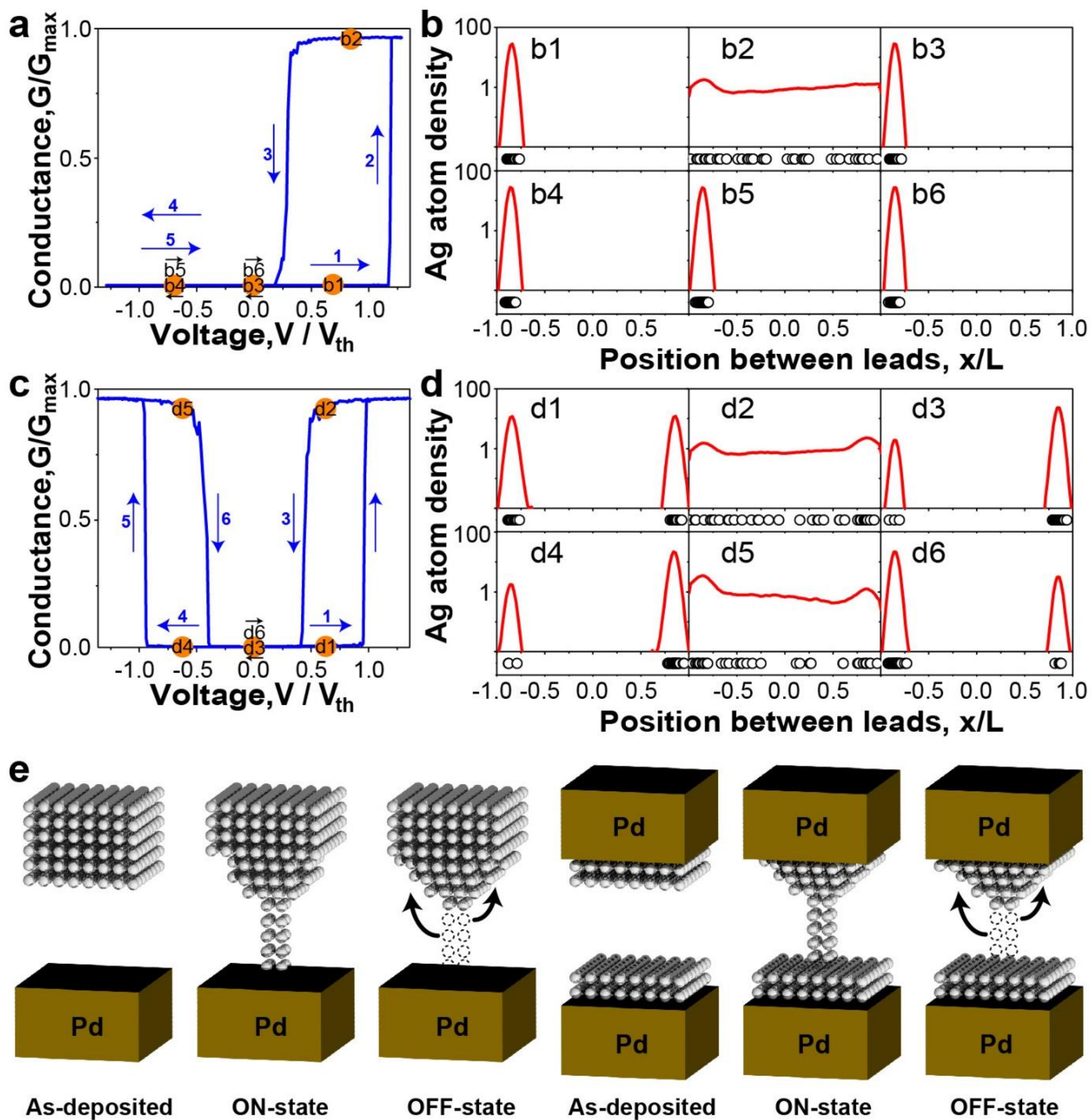

Figure 5